Considering Various Multimoment Bulk Microphysics Schemes for Simulation of Passive Microwave Radiative Signatures

Jiseob Kim, Dong-Bin Shin, and Donghyeck Kim

Abstract—**Passive microwave radiative transfer models are strongly influenced by the cloud and precipitation hydrometeor properties. Particularly, they can sensitively interact with frozen hydrometeors through multiple high-frequency channels. However, frozen hydrometeors are one of the most difficult parameters to comprehend due to the lack of *in situ* data. Until recently, studies have attempted to describe more reasonable hydrometeor distributions using various microphysics parameterizations coupled with the weather research and forecasting (WRF) models. Herein, we aim to apply the proposed methods to passive microwave radiative transfer simulations. We implemented a passive microwave radiative transfer simulation that considers various microphysical assumptions by creating a new Mie scattering lookup table. Furthermore, we evaluated the bulk microphysics parameterizations [WDM6, Morrison (MORR), Thompson (THOM), and P3 schemes] for the tropical cyclone Krosa (2019) that were observed by the global precipitation measurement microwave imager instrument, specifically concentrating on the rimed and aggregated ice categories (snow, graupel, and P3 ice). Based on the evaluation results, we concluded the following: WDM6 graupel and MORR snow afford excessive scattering signals at 37 GHz. However, at 166 GHz, none of the parameterizations produces sufficient scattering signals for comparison with the observations. The P3 ice affords significantly underestimated scattering signals at 89 GHz and above, despite its sophisticated assumptions. On the contrary, THOM snow affords scattering signals similar to the observations, despite a shape-related error. In summary, this study introduced a method for implementing a microphysical-consistent radiative transfer computation and successfully showed how various microphysical assumptions of clouds can change the passive microwave radiative signatures.**

Index Terms—**Microphysical assumption, microphysics parameterization, microwave radiometry, passive microwave radiative transfer model (RTM).**

I. INTRODUCTION

NUMERICAL weather prediction (NWP) models play an important role in the perception of the precipitation structures and processes, especially in areas where *in situ* observation data are rare. The models simulate cloud and precipitation processes on a grid scale using microphysics parameterization, which can be classified into two different

approaches: spectral (bin) microphysics and bulk microphysics scheme (hereinafter, bulk scheme). The former solves explicit microphysical equations to calculate the number concentration of hydrometeors on a finite difference diameter bin, whereas the latter approximates the particle size distributions (PSDs) as a function of exponential, gamma, or lognormal distributions. Since PSDs can be easily determined using a few prognostic variables, the bulk scheme exhibits good computational efficiency (for more information on microphysics parameterization, see [1]).

Various bulk schemes, including [2]–[6], have been proposed based on different field campaigns to simulate a realistic hydrometeor distribution. Moreover, the bulk schemes have been improved by adjusting the microphysical assumptions (e.g., shape, density, and PSD) and adding other prognostic variables. Although these approaches have been numerically validated in various ways over the years, bulk schemes are still one of the most uncertain physical processes in NWP models. Herein, we evaluate the microphysical assumptions of various bulk schemes using microwave remote sensing observations and a signal-based evaluation.

Microwave radiative transfer models (RTMs) are reasonably appropriate tools for evaluating and improving the bulk schemes because microwave radiation can penetrate clouds, unlike infrared or visible light that cannot penetrate the cloud top. When radiation propagates, some of it is absorbed, emitted, or scattered by liquid water droplets and ice particles. This denotes that microwave RTMs require predefined microphysical assumptions, such as species, shape, density, and PSD of the hydrometeors. According to [7], these assumptions, defined by the bulk schemes, can cause significant changes in the radiance calculation of microwave RTMs. Therefore, when using an RTM together with an NWP model, the resolution of the mismatch in the microphysical assumptions between them is considered an important issue. Thus, to minimize the microphysical uncertainties, the assumptions of the RTM should be as close as possible to those of the NWP model, as mentioned in the studies of [8]–[12].

Numerous studies, including [9], [10], and [13]–[21], have carried out signal-based evaluations using radar simulators and passive microwave RTMs considering the coincident microphysical assumptions. However, most studies have focused on reflectivity analysis using the radar simulator. Additionally, a new type of bulk scheme [5] has been recently proposed that allows flexible ice density, but it has not yet been addressed

from the passive microwave perspective. The current satellite-based passive microwave instruments possess multiple high-frequency channels (30–200 GHz) that are sensitive to ice particles, ranging from small to large sizes, and they allow the in depth analysis of ice PSDs. Therefore, we implement a passive microwave radiative transfer simulation that considers various microphysical assumptions, including the recently proposed flexible ice density. Its microphysical assumptions fully match the bulk schemes used herein.

In this radiative transfer simulation, ice particles are generally assumed to be spherical since it is based on the Mie assumption, which causes simulation errors due to an inadequate representation of both particle shape and dielectric constant [22]. In particular, for ice particles larger in size than the wavelength of the light, the internal structure becomes important, and the errors increase. Fortunately, large aggregates of multiple ice crystals tend to have a low density, which can partially reduce the errors (see [23], [24]). In the past few years, many studies [25]–[29] have investigated the potential uncertainty of the Mie assumption using the simulation of passive microwave radiances. In the experiments, spherical particles are set to have a constant density, but nonspherical particles are generally characterized by a diameter-dependent density. Thus, some parts of the presented errors for the Mie assumption are probably due to the constant density assumption. In fact, the shape-related error is considered to be relatively smaller than other microphysical assumptions such as PSD and density [30]. Furthermore, Geer and Baordo [31] mentioned that a description of nonspherical particles can yield other errors because their exact shape and orientation must be arbitrarily estimated. Therefore, this study adopts the Mie assumption for the radiative transfer simulation, despite the potential error.

This study aims to evaluate various microphysical assumptions, such as single-moment scheme, double-moment scheme, and unfixed density, using the microphysical-consistent passive microwave RTM. English *et al.* [12] noted that the recent increase in high-performance computing nodes has enabled the employment of sophisticated microphysical assumptions. Major improvements in bulk schemes are concentrated on frozen hydrometeors, such as snow and graupel, subsequently increasing the need for passive microwave RTM. Furthermore, a passive microwave RTM as an observation operator is essential for all-sky satellite data assimilation, a significant challenge of NWP centers. The utilization of cloud- and precipitation-affected radiance for data assimilation would help in comprehending cloud and precipitation processes and acquiring accurate data, as mentioned in [32], [33].

This article is organized as follows. Section II describes the construction of the radiative transfer simulation and the methodology for calculating the Mie scattering parameters. Section III describes the bulk microphysics schemes employed and their microphysical assumptions. In Section IV, the bulk schemes are evaluated using the radiative transfer simulation for a specific precipitation case observed using a satellite sensor and the differences caused by the microphysical assumptions are discussed. Finally, a conclusion is provided in Section V.

II. RADIATIVE TRANSFER SIMULATION

Herein, the passive microwave radiative transfer simulation is based on the Eddington approximation in a plane–parallel medium of [34]. Moreover, the atmospheric transmittance by absorbing gases (O_2, H_2O, and N_2) is calculated through the widely used millimeter wave propagation model 1993 of [35], and the ocean surface emissivity is obtained from the results of a fast microwave emissivity model (FASTEM; [36]) version 6 (FASTEM-6). FASTEM-6 is also used in the latest versions of the radiative transfer for the television infrared observation satellite (TIROS) operational vertical sounder (RTTOV; [37]) and the community RTM (CRTM; [38], [39]) developed at the joint center for satellite data assimilation. The scattering and absorption by clouds are computed based on the Mie solution described in [40]–[42] and are then modified using a profile average cloud fraction to consider the subgrid scale variability (refer to [43]).

The Mie solution determines parameters such as scattering coefficient, K_{sca}, absorption coefficient, K_{abs}, and asymmetry factor, g, which can be described as follows:

$$K_{\text{sca}} = \int_0^\infty N(D)\sigma_{\text{sca}} dD \tag{1}$$

$$K_{\text{abs}} = \int_0^\infty N(D)\sigma_{\text{abs}} dD, \quad \text{and} \tag{2}$$

$$g = \frac{1}{K_{\text{sca}}} \int_0^\infty g(D)N(D)\sigma_{\text{sca}} dD \tag{3}$$

where σ_{sca} (σ_{abs}) is the scattering (absorption) cross-sectional area, which is related to the scattering (absorption) efficiency factor. The efficiency factor can be derived using the size parameter, x, and the complex refractive index, m, which is relative to the particle density, ρ. The function, $g(D)$, denotes the integral sum of the phase function in all directions. The particle number concentration, $N(D)$, is the number of particles in a given diameter, ranging from D to $D + dD$. In bulk microphysics schemes, the size distribution is generally represented through some continuous probability distribution parameters.

This study implements the passive microwave radiative transfer simulation with various bulk schemes by varying the microphysical assumptions needed for the Mie calculation. In other words, the Mie calculation results are provided for a variety of microphysical assumptions. The Mie solution is a powerful analytical method used to solve Maxwell's equations for spherical particles; however, it is computationally heavy as complicated calculations must be carried out for every grid and layer in which the particles exist. Thus, the burden on the entire model would increase if any bulk scheme requires a large amount of computations. Hence, this study adopts a fast model approach using a precomputed lookup table (LUT).

The LUT can be represented using a multidimensional matrix, usually comprising frequency, temperature, hydrometeor type, and mass mixing ratio, q. However, CRTM employs an effective radius instead of q. Remarkably, the variables here may be different for each bulk scheme and hydrometeor type, denoting that numerous variables may be required to fully describe complicated microphysical assumptions.

TABLE I

VARIABLES DETERMINING THE SIZE DISTRIBUTIONS OF LIQUID WATER DROPLETS AND ICE PARTICLES IN THE FIVE BULK SCHEMES. THE SUBSCRIPTS INDICATE THE ABBREVIATIONS FOR THE HYDROMETEORS (c: CLOUD WATER, r: RAIN, i: CLOUD ICE, s: SNOW, AND g: GRAUPEL)

Scheme	Cloud water	Rain	Cloud ice	Snow	Graupel
WDM6	q_c, $N_{tot,c}$	q_r, $N_{tot,r}$	q_i	q_s, T	q_g
MORR	q_c, fixed $N_{tot,c}$	q_r, $N_{tot,r}$	q_i, $N_{tot,i}$	q_s, $N_{tot,s}$	q_g, $N_{tot,g}$
THOM	q_c, fixed $N_{tot,c}$	q_r, $N_{tot,r}$	q_i, $N_{tot,i}$	q_s, T	q_g, T, q_r, $N_{tot,r}$
P3 1ICE	q_c, fixed $N_{tot,c}$	q_r, $N_{tot,r}$	q_i, $N_{tot,i}$, q_{rime}, B_{rime}		
P3 2ICE	q_c, $N_{tot,c}$	q_r, $N_{tot,r}$	two pairs of q_i, $N_{tot,i}$, q_{rime}, B_{rime}		

Matsui *et al.* [15] emphasized that this could be a significant advantage for radiance-based model evaluation because it enabled the evaluation of detailed aspects of microphysical assumptions. Herein, all the variables (e.g., total number concentration, N_{tot}, and rimed ice-related prognostic variables) required by bulk schemes to describe their microphysical assumptions are added. Although this optimization is often neglected because of its complexity, it is essential for creating a set of LUTs to minimize the errors associated with the microphysical assumptions. Moreover, the range and bin size of the elements are restricted to prevent the LUTs from becoming too large. The particle diameter ranges are as follows: 1–250 μm for every 1 μm (cloud water), 100 μm–9 mm for every 20 μm (rain), 1 μm–1.5 mm for every 5 μm (cloud ice and unrimed ice), and 2 μm–5 cm for every 100 μm (snow, graupel, and rimed ice). Furthermore, the prognostic variables, including q and N_{tot}, are limited to 50 bins. The temperature range is limited from 230 to 310 K for every 4 K for the liquid water droplets and from 222 to 270 K for every 12 K for the ice particles. As is known, the real part of the refractive index of ice has a definite value in the microwave region, but the imaginary part slightly varies depending on the temperature. Additionally, to define PSD, some bulk schemes require the temperature. Therefore, the temperature cannot be fixed for ice particles. The construction of a multidimensional LUT affords considerable computational costs. However, once completed, no significant difference is observed in the time required to run the RTM. Thus, the implemented RTM is not only consistent with the microphysical assumptions of bulks schemes but also applicable to diverse fields.

III. MICROPHYSICS PARAMETERIZATIONS

This study evaluates five bulk schemes: the weather research and forecasting (WRF) double-moment six-class (WDM6; [4]) scheme, the Morrison double-moment (MORR; [2]) scheme, the Thompson (THOM; [3]) scheme, the predicted particle properties (P3) with a single free ice category (P3 1ICE; [5]) scheme, and the P3 with a double free ice category

(P3 2ICE; [6]) scheme. The first three schemes comprise two liquid water droplets (cloud water and rain) and three ice particles (cloud ice, snow, and graupel) categories, while the last two P3 schemes do not classify the ice based on appearance. The P3 schemes merge all ice categories (small ice, unrimed ice, spherical graupel, and partially rimed ice) into the single or double free ice category. They possess two advantages: they are free from unnatural assumptions, such as a fixed density, and are computationally efficient, which is only for the single free ice category.

Table I shows the variables controlling the PSD of the bulk schemes employed herein. They are also the elements required to fabricate the Mie LUTs. To determine the size distribution, the liquid water droplets of the WDM6 scheme must have a combination of q and N_{tot}, which are the prognostic variables, whereas the ice particles do not require N_{tot}. This implies that, in this instance, N_{tot} is simply diagnosed by integrating the PSD. On the contrary, the MORR scheme requires N_{tot} for all hydrometeor categories. Additionally, the THOM graupel requires the rain mass mixing ratio q_r and rain total number concentration $N_{tot,r}$ instead of its own $N_{tot,g}$ to fully describe its PSD. Finally, the P3 schemes require four variables per ice class: the ice mass mixing ratio, q_i, ice total number concentration, $N_{tot,i}$, rime mass mixing ratio, q_{rime}, and rime volume mixing ratio, B_{rime}. Therefore, bulk schemes determine their size distribution in different ways, which our model fully considers.

This study concentrates on the rimed and aggregated ice categories (snow, graupel, and P3 ice), which can well scatter the high-frequency microwave radiation. Uncertainties associated with the frozen hydrometeors are also a major improvement goal in both the bulk scheme and RTM research fields. Although rain droplets are accepted as one of the important scatterers in the microwave radiation region, the scattering due to them could be offset by their own absorption and emission. In other words, their net scattering is of little importance than that of the ice categories. Detailed descriptions of the microphysical assumptions are discussed in Sections III-A and

TABLE II
MASS–DIAMETER RELATIONSHIPS AND PARTICLE DENSITIES FOR THE P3 ICE CATEGORIES. BOUNDARIES BETWEEN SMALL ICE AND
UNRIMED ICE, UNRIMED ICE AND SPHERICAL GRAUPEL, AND SPHERICAL GRAUPEL AND PARTIALLY RIMED ICE ARE
DEFINED AS D_{th}, D_{gr}, AND D_{cr}, RESPECTIVELY

Ice category	α [kg/m$^\beta$]	β	Density [kg/m^3]
Small ice	$(\pi\rho_i)/6$	3	917
Unrimed ice	$\alpha_{va} = 0.0121$	$\beta_{va} = 1.9$	$\dfrac{6\alpha_{va}}{\pi} D^{\beta_{va}-3}$
Spherical graupel	$(\pi\rho_g)/6$	3	$\rho_{rime}F_{rime}$ $+ (1 - F_{rime})\dfrac{6\alpha_{va}(D_{cr}{}^{\beta_{va}-2} - D_{gr}{}^{\beta_{va}-2})}{\pi(\beta_{va} - 2)(D_{cr} - D_{gr})}$
Partially rimed ice	$\left(\dfrac{\alpha_{va}}{1 - F_{rime}}\right)$	β_{va}	$\dfrac{6\alpha_{va}}{\pi(1 - F_{rime})} D^{\beta_{va}-3}$

III-B. Herein, the microphysical assumptions information is obtained from the related literature of [2]–[6] and [44]–[46], and the physics code of the WRF version 4.1.5 model is used as a reference.

A. Mass–Diameter Relationships

The mass–diameter relationship generally exhibits a standard power law form

$$\text{mass}(D) = \alpha D^{\beta} \qquad (4)$$

where the constant α is equal to $(\pi\rho)/6$ and the exponent β is equal to 3 if the particle is spherical. Thus, the relationship is related to the bulk density of the particle. The density for the liquid water droplets is assumed to be approximately 1000 kg/m^3 in most bulk schemes, except the MORR scheme (997 kg/m^3). Ice particles can be defined with different densities depending on their type: 917 kg/m^3 for cloud ice, 100 kg/m^3 for snow, and 400 or 500 kg/m^3 for graupel. However, not all bulk schemes always assume spherical particles. Our model considers a nonspherical particle (e.g., aggregated particles) as a spherical particle with its maximum length (D_{max}) as the diameter (Fig. 1). Its density is defined by the mass–diameter relationship ($\rho = (6/\pi)\alpha D^{\beta-3}$), and then the particle is considered as a soft sphere consisting of a homogeneous ice–air mixture. For example, the THOM scheme assumes that snow comprises nonspherical fractal-like aggregated crystals, i.e., $\alpha = 0.069$ kg/m^2 and $\beta = 2$, as shown in [3] and [47]. Consequently, instead of being fixed, the density decreases according to the diameter. The mixture assumption is generally valid when the particle size is smaller than the wavelength of the light. In the opposite case, it may cause some errors in the dielectric constant. Fortunately, a low density of the large particles makes the errors less important. The P3 schemes diagnose the density of the ice categories using prognostic variables. Specifically, both the rime fraction ($F_{rime} = Q_{rime}/Q_i$) and rime mass
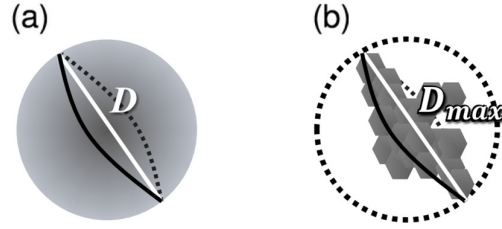

Fig. 1. Descriptions of (a) spherical particle and (b) nonspherical aggregated particle. D is the diameter of the spherical particle and D_{max} is the maximum length of the aggregated particle.

density ($\rho_{rime} = Q_{rime}/B_{rime}$) determine the density of rimed ice particles. Table II shows the mass–diameter relationships and the densities of the P3 schemes. The four ice categories are distinguished by their boundary diameters (D_{th}, D_{gr}, and D_{cr}). Here, D_{th}, D_{gr}, and D_{cr} are the critical diameter separating small ice and unrimed ice, unrimed ice and spherical graupel, and graupel and partially rimed ice, respectively. The unrimed ice and partially rimed ice densities inversely vary with the diameter similar to the THOM snow. On the contrary, the spherical graupel density is independent of the diameter; instead, it includes D_{gr} and D_{cr} obtained via the numerical iteration method (see [5], [48]). Its density, ρ_g, is obtained at the end of the iteration.

Fig. 2 shows the relationship between the bulk particle density and diameter with the size parameter at 89 GHz. In the radiative transfer simulation, the intensity of scattering by any particle is determined by multiplying the size parameter and refractive index obtained using the density. The THOM snow density (bold solid curve) demonstrates the exponential decay along the diameter. When the diameter exceeds about 1.32 mm, the THOM snow density is limited to less than 100 kg/m^3. This implies that the THOM scheme assumes a low scattering efficiency for snow particles with diameters greater than 1.32 mm. On the contrary, if the particle size is less than 1.32 mm, the snow density is significantly

TABLE III

PSD INTERCEPT PARAMETERS (N_0; m^{-4}) FOR THE RIMED AND AGGREGATED ICE CATEGORIES (SNOW, GRAUPEL, AND P3 ICE). α_x AND β_x ARE DEFINED BY THE MASS–DIAMETER RELATIONSHIPS IN TABLE II, AND ρ_a IS THE AIR DENSITY. IN THE THOM SCHEME, $N_{0,\text{exp}}$ IS A CORRECTION TERM WHICH REFLECTS THE EFFECTS OF RAIN DROPLETS

Scheme	Intercept parameter for snow N_{0s}	Intercept parameter for graupel N_{0g}
WDM6	$2e6 \times MAX[MIN[e^{0.12(273.15-T)}, 5e4], 1]$	$4e6$
MORR	$N_{tot,s}(\dfrac{\alpha_s N_{tot,s}\Gamma(\beta_s+1)}{\rho_a q_s})^{\frac{1}{\beta_s}}$	$N_{tot,g}(\dfrac{\alpha_g N_{tot,g}\Gamma(\beta_g+1)}{\rho_a q_g})^{\frac{1}{\beta_g}}$
THOM	$490.6\dfrac{M_2^{\,4}}{M_3^{\,3}}$	$N_{0,exp}(\dfrac{\Gamma(\beta_g+1)}{(\beta_g+1)})^{\frac{1}{\beta_g}}$

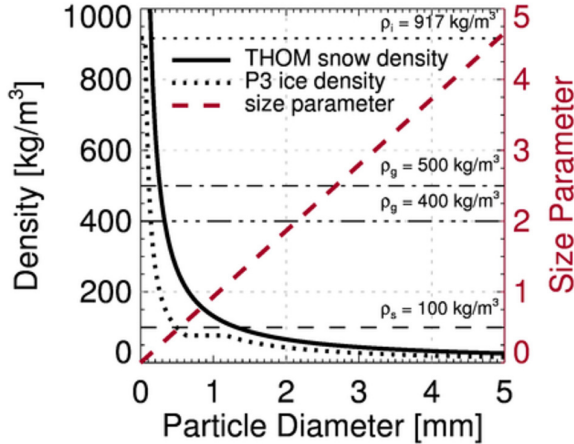| Scheme	Intercept parameter for P3 ice N_{0i}
P3	$\dfrac{\rho_a q_i}{\int_0^{D_{th}} \alpha_1 D^{\beta_1+\mu} e^{-\lambda D} dD + \int_{D_{th}}^{D_{gr}} \alpha_2 D^{\beta_2+\mu} e^{-\lambda D} dD + \int_{D_{gr}}^{D_{cr}} \alpha_3 D^{\beta_3+\mu} e^{-\lambda D} dD + \int_{D_{cr}}^{\infty} \alpha_4 D^{\beta_4+\mu} e^{-\lambda D} dD}$

Fig. 2. Density plot with respect to the particle diameter. Thin lines represent the fixed densities. The bold solid curve denotes the THOM snow density, and the bold dotted curve indicates the P3 ice density. The P3 ice density depends on the prognostic variables (here, $F_{\text{rime}} = 0.5$ and $\rho_{\text{rime}} = 100$ kg/m^3). The size parameter (red dashed line) is described only for 89 GHz.

greater than 100 kg/m^3. Moreover, the excessive scattering is balanced by the size parameter (red dashed line). These particles simply mimic the contribution of high-density ice particles (cloud ice, graupel, and/or hail) to scattering. The P3 ice density (bold dotted curve) tends to be similar to the THOM snow density, but the continuous curve comprises up to four independent formulae (Table II). Fig. 2 shows that the THOM snow density is greater than the P3 ice density in the entire diameter range. However, this may not be true if many high-density rimes are present. This is entirely dependent on the prognostic variables, implying that the density of P3 ice is significantly more flexible than that of the other ice categories. Morrison *et al.* [46] noted that this approach was effective

for simulating a result similar to that of the observed radar reflectivity products.

B. Particle Size Distributions

PSD is commonly approximated to the generalized gamma distribution form

$$N(D) = N_0 D^{\mu} e^{-\lambda D} \tag{5}$$

where N_0 is the intercept, λ is the slope, and μ is the shape parameter. If μ is zero, the gamma distribution is an exponential distribution. Equation (5) can easily describe various types of distributions using only the above three parameters. However, inappropriate parameter assumptions, due to a lack of information, could afford errors for both bulk schemes and RTMs.

PSD parameters are represented by a fixed value or function of the prognostic variables through a momentum relation. The nth moment M_n of the size distribution can be expressed as follows:

$$M_n = \int_0^{\infty} D^n N(D) dD \tag{6}$$

where the zeroth moment M_0 and third moment M_3 are associated with N_{tot} and q, respectively. A method predicting only the third moment is called a single-moment scheme, whereas a method predicting both the zeroth and third moments is called a double-moment scheme. For snow and graupel, the WDM6 and THOM schemes are single-moment schemes while the MORR scheme is a double-moment scheme. The P3 schemes are double-moment schemes for the ice species. The double-moment approach well represents N_0 as it does not limit N_0 to a fixed value. Understandably, a fixed N_0 is a major cause of unrealistic PSD.
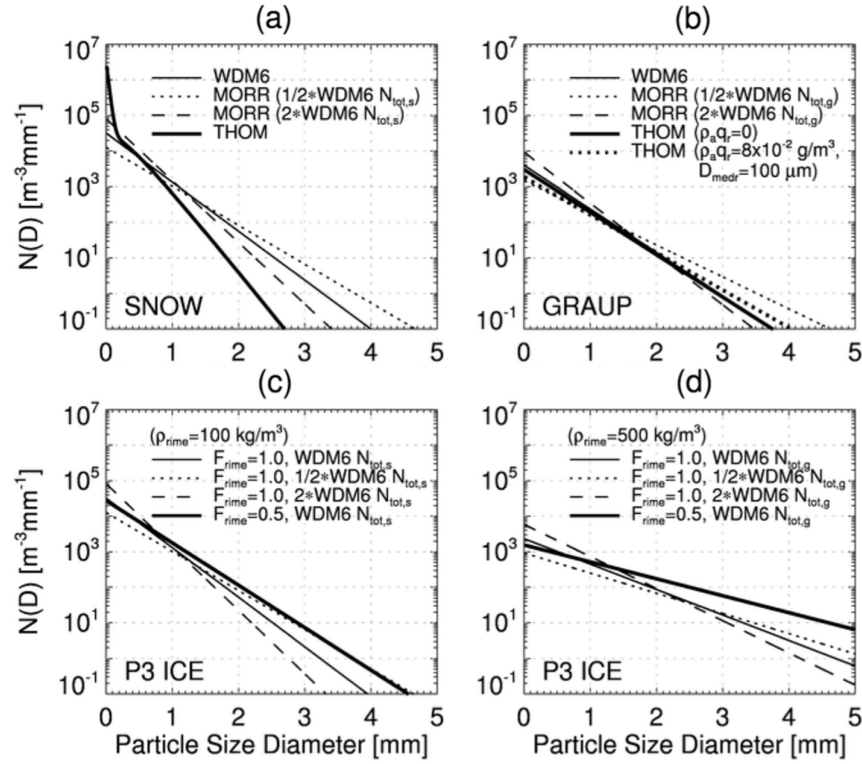
Fig. 3. Ice PSDs for the bulk schemes. The first row describes the representative distributions of (a) snow and (b) graupel for the WDM6, MORR, and THOM schemes. The second row shows the P3 ice distributions at (c) $\rho_{\text{rime}} = 100$ kg/m^3 and (d) $\rho_{\text{rime}} = 500$ kg/m^3. The water content, q_x, and temperature are assumed to be 0.1 g/m^3 and 250 K, respectively. For the double-moment schemes, the total number concentration is replaced by $N_{\text{tot},x}$ diagnosed by the WDM6 scheme. In addition, half (twice) the value of $N_{\text{tot},x}$ is illustrated by the dotted (dashed) lines.

However, this does not imply that single-moment schemes perform poorly. Recent single-moment schemes often define N_0 in their own unique ways. Table III shows how bulk schemes define N_0 for the rimed and aggregated ice categories. WDM6 snow assumes that N_{0s} depends on the layer temperature T. THOM snow is a little more complicated. Its N_{0s} is determined by the second moment, M_2, and the third moment, M_3. Based on the moment parameterization presented in [49] and [50], the nth moment can be approximated as a function of temperature in degrees Celsius T_c and M_2: $M_n = A(n)\exp[B(n)T_c]M_2^{C(n)}$. Here, $A(n)$, $B(n)$, and $C(n)$ are quadratic functions of only n (for more information, refer to [50]). Since the THOM snow mass is proportional to the square of the diameter ($\beta = 2$), M_2 is related to q_s. Consequently, N_{0s} of the THOM snow is simply a function of T_c and q_s. On the contrary, for graupel, THOM's N_{0g} includes an additional term $N_{0,\exp}$ to reflect the effect of rain drops using q_r and $N_{\text{tot},r}$. Only WDM6 graupel employs a fixed N_0.

In a double-moment scheme, N_0 is usually controlled using both q and N_{tot}, of which the MORR scheme is a typical example. On the contrary, the recently proposed P3 scheme requires all four prognostic variables to define N_{0i}, and the numerical iteration method is again required to obtain it.

Fig. 3 shows the PSDs for the employed bulk schemes. The water content ($=\rho_a q$, where ρ_a is the air density) and temperature are fixed as 0.1 g/m^3 and 250 K, respectively, to maintain identical conditions. In the double-moment schemes, N_{tot} is temporarily replaced by the N_{tot} ($=N_0/\lambda$) identified by the WDM6 scheme. Fig. 3 shows the following

remarkable features. First, under the same water content, compared to single-moment schemes, double-moment schemes can describe more flexible distribution forms through the predicted N_{tot}. Furthermore, a relatively large value of N_{tot} (dashed lines) yields numerous small particles and a few large particles, and vice versa. Note that the distinction between large and small particles is relatively determined by their own PSD. Second, the THOM scheme exhibits a significantly high quantity of small-sized snow [bold solid line in Fig. 3(a)]. The unique shape of the distribution is because of the super-exponential distribution that comprises exponential and gamma functions, which well matches the aircraft data introduced in [49]. Third, the THOM graupel distribution [bold lines in Fig. 3(b)] is affected by the presence of rain droplets, which is described by the rain median mass diameter D_{medr} and rain water content $\rho_a q_r$ in the same space and time. The rain droplets decrease the small-sized graupel and increase the large-sized graupel. Finally, the P3 scheme [Fig. 3(c) and (d)] shows various PSD form possibilities through multifarious combinations of the prognostic variables. The four variables (q_i, $N_{\text{tot},i}$, q_{rime}, and B_{rime}) are fully involved in determining N_{0i}, λ_i, and μ_i. Particularly, the variables associated with rime are important here. They determine the PSD as well as the particle density. The number of large (small) particles decreases and the density of large (small) particles increases with increasing rime fraction (rime density). Furthermore, if λ_i exceeds a specific value (~ 5960.33 m^{-1}), μ_i becomes greater than zero, switching the shape to a gamma distribution (not shown here). Morrison and Milbrandt [5] stated that the proposed approach

is highly realistic. However, this approach has an inherent limitation (called "dilution problem"): a sufficient number of large particles is not present. This is because only one ice category exists in the same space and time. Therefore, the P3 2ICE with two free ice categories has been suggested as a solution. This study verifies whether P3 2ICE well solves the dilution problem.

IV. EVALUATION OF THE MICROPHYSICS SCHEMES

A. WRF Simulation

The input variables of the passive microwave radiative transfer simulation were simulated using the WRF version 4.1.5 model. The initial and boundary conditions were obtained from the national centers for environmental prediction final dataset on 1.0° grids and an interval of 6 h. The WRF model was configured with three domains (36, 12, and 4 km), 32 vertical levels up to a 50 hPa pressure top, and a fixed time step of 180 s for integration. Physics parameterization includes the Kain–Fritsch cumulus scheme (turn off for the third domain) and the Yonsei University surface and planetary boundary layer scheme. With these configurations, the five bulk schemes (WDM6, MORR, THOM, P3 1ICE, and P3 2ICE) were sequentially applied.

Herein, we simulated a tropical cyclone "Krosa" that formed in the northwestern Pacific Ocean on August 5, 2019. The WRF model created a 36-h forecast from 00:00 UTC August 6, 2019 to 12:00 UTC August 7, 2019. During this time, the global precipitation measurement (GPM) microwave imager (GMI) instrument passed over the area once. The area (latitude: 16°N–24°N and longitude: 138°E–146°E) and time (03:40 UTC August 7, 2019) were selected for analysis.

Note that the five different bulk schemes not only cause different microphysical properties but also different storm intensities and locations. We have analyzed the intensity (in terms of minimum pressure) biases and center location errors for the simulated tropical cyclones. First, we have obtained the tropical cyclone best track data at 6-h intervals from the joint typhoon warning center (JTWC). Second, we have derived the simulated tropical cyclone center positions using the Geophysical Fluid Dynamics Laboratory (GFDL) vortex tracker (for the detailed how-tos, refer to [51]). Finally, the intensity biases and location errors were derived after the best track data were interpolated to GMI observation times (03:40 UTC August 7, 2019). The intensity biases are as follows: 5.73 hPa for WDM6, 0.53 hPa for MORR, 1.15 hPa for THOM, −1.69 hPa for P3 1ICE, and −1.66 hPa for P3 2ICE and the location errors are as follows: 87.1 km for WDM6, 85.6 km for MORR, 75.5 km for THOM, 7.7 km for P3 1ICE, and 83.8 km for P3 2ICE.

Storm intensity biases and location errors have been reported by various studies through microphysics sensitivity tests using WRF simulations. Li and Pu [52] showed the maximum intensity difference of 23 hPa at the end of the 30-h storm forecast. The experiments also showed the center location errors of up to 97 km. Furthermore, Tao *et al.* [53] presented previous modeling studies on the impact of microphysics

schemes on storm intensity and location. The presented intensity and location errors were similar to those of [52]. In an effort to reduce the effects on the errors, we used a latitudinal average over 16°N–24°N. This helped in focusing on the comparison of the hydrometeor distributions and refining their major scattering effects by reducing the location differences in the latitudinal direction. However, the following radiance comparison results include some of the effects of the intensity errors. Fortunately, the intensity errors are generally smaller than those of the previous studies (see [52], [53]). Herein, we did not treat intensity differences as important, because they are not our main concern.

Figs. 4 and 5 show the vertical cross sections of the ice water contents (filled contours) and their vertically integrated columns, i.e., the ice water path, (solid line plots) simulated by the WRF model. In Fig. 4, the bulk schemes simulate different amounts of water content due to the differences in their intrinsic assumptions associated with the microphysical processes. The THOM scheme simulated the highest amount of snow water content (<0.89 g/m^3), followed by the MORR (<0.76 g/m^3) and WDM6 (<0.39 g/m^3) schemes [Fig. 4(a)–(c)]. The opposite trend was observed for graupel [Fig. 4(d)–(f)]. The WDM6 scheme possessed a significantly higher graupel water content (<0.50 g/m^3) than the other schemes (MORR scheme: <0.21 g/m^3 and THOM scheme: <0.18 g/m^3). The obtained results are similar to those previously reported in [18], [20], and [54].

Fig. 5 is similar to Fig. 4, but it describes the P3 ice water content. Fig. 5(a) shows the total water content of all ice species, from the small ice to the spherical graupel. Fig. 5(b) and (c) shows two free ice categories afforded by the P3 2ICE scheme: ice1 and ice2. Ice1 in the P3 1ICE scheme contained a higher water content (<0.85 g/m^3) than the ice1 (<0.64 g/m^3) in the P3 2ICE scheme, especially at the convection center. Milbrandt and Morrison [6] stated that the properties of the two ice categories at any given point may be different. Thus, ice1 and ice2 are represented by different types of density and PSD, although they are basically based on the same microphysics.

In the WRF model, the simulated prognostic variables including ice water mixing ratio (or ice water content) determine the PSD parameters (intercept, slope, and shape). As shown in Figs. 6 and 7, we described ranges of the actual ice PSDs after the application of all prognostic variables assigned to each model grid cell for the tropical cyclone (03:40 UTC August 7, 2019). Fig. 6 shows that the MORR scheme is relatively easy to have large-sized snow particles, while the THOM scheme is not. The THOM scheme is also difficult to have large-sized graupel particles, probably because of the lowest graupel water content. Similarly, Fig. 7 shows the actual P3 ice PSDs. Note that they include all ice species (cloud ice, unrimed ice, spherical graupel, and partially rimed ice). There is a meaningful difference between the ice1 particles of the P3 1ICE and 2ICE scheme. The latter can grow to larger sized-particles than the former, reducing the dilution problem of the one-category version. This improvement has been made possible by assuming the additional ice category (ice2) that plays a complementary role. In the next step,
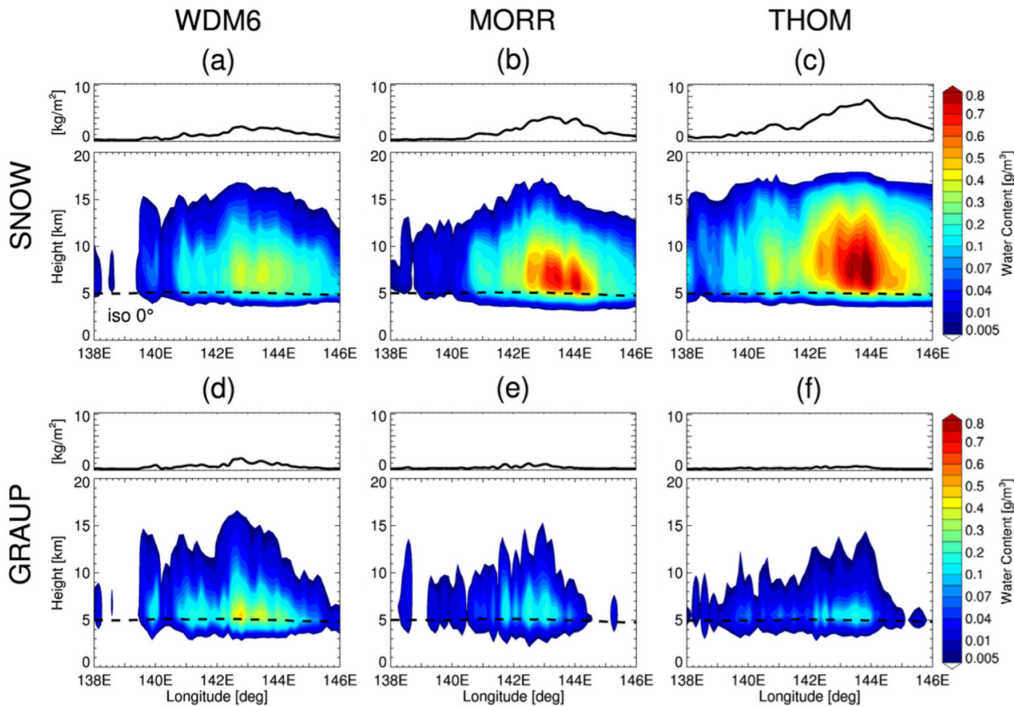
Fig. 4. Latitudinal averages (16°N–24°N) of the vertical cross section of the water content (filled contour) and the ice water path (line plot) simulated by the bulk schemes (left: WDM6, middle: MORR, and right: THOM) for the tropical cyclone (03:40 UTC August 7, 2019). The first row indicates the snow content, while the second row indicates the graupel content. The minimum contour level is set to 0.005 g/m³. The dashed line denotes the freezing level (zero-degree isotherm).
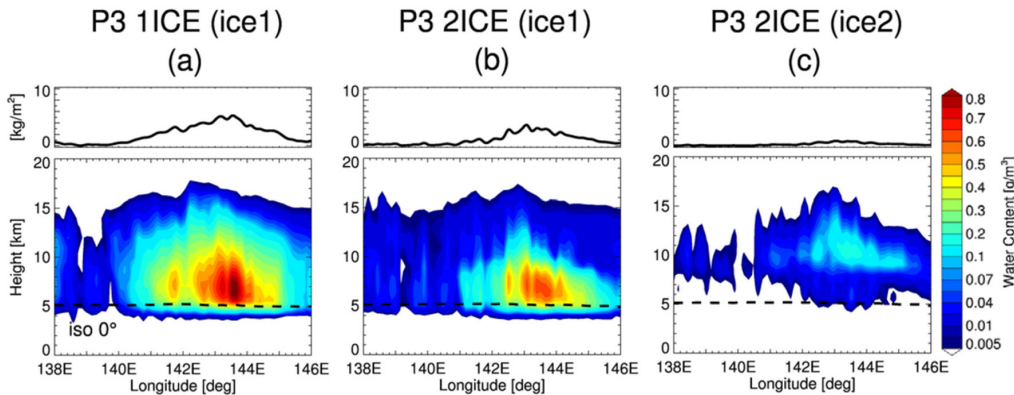

Fig. 5. Similar to Fig. 4, but for the free ice categories in the P3 scheme. (a) Left thing illustrates the single free category in the P3 1ICE scheme. (b) Middle and (c) right images represent the first (ice1) and the second (ice2) free ice categories, respectively, in the P3 2ICE scheme.

we mainly focused on their scattering signal differences in the microwave region.

B. Microwave Scattering by Snow, Graupel, and P3 Ice

We analyzed the brightness temperature (TB) depressions simulated by the microphysical-consistent radiative transfer computation for the tropical cyclone event shown in Figs. 4 and 5. First, the TB values were calculated using a single hydrometeor (snow, graupel, or P3 ice) by artificially turning off the other hydrometeors. The results showed the differences in scattering caused by the inherent assumptions of each hydrometeor.

Out of the 13 channels of the GPM GMI sensor, high-frequency imager channels (37, 89, and 166 GHz) are closely associated with scattering. Furthermore, the scattering process is governed by the size parameter, which is inversely proportional to the wavelength ($x = (D\pi)$/wavelength). In other words, for the same size parameter, the 37-GHz channel requires a larger particle size than the 166-GHz channel. For example, if the size parameter $x = 0.2$, the particle diameters for the 37, 89, and 166 GHz channels are about 0.52, 0.21, and 0.11 mm, respectively. Thus, a higher frequency channel could be more effectively scattered by smaller particles. This allows the evaluation of the microphysical assumptions across different particle size ranges. Therefore, we mainly used three high-frequency channels, especially vertical polarization (V-pol). The results, like Figs. 4 and 5, were averaged in the latitudinal direction, and they are shown in Fig. 8.

Fig. 8(a)–(c) shows the TB reduction by snow (or ice1 for P3). Clearly, the scattering signals by the ice particles
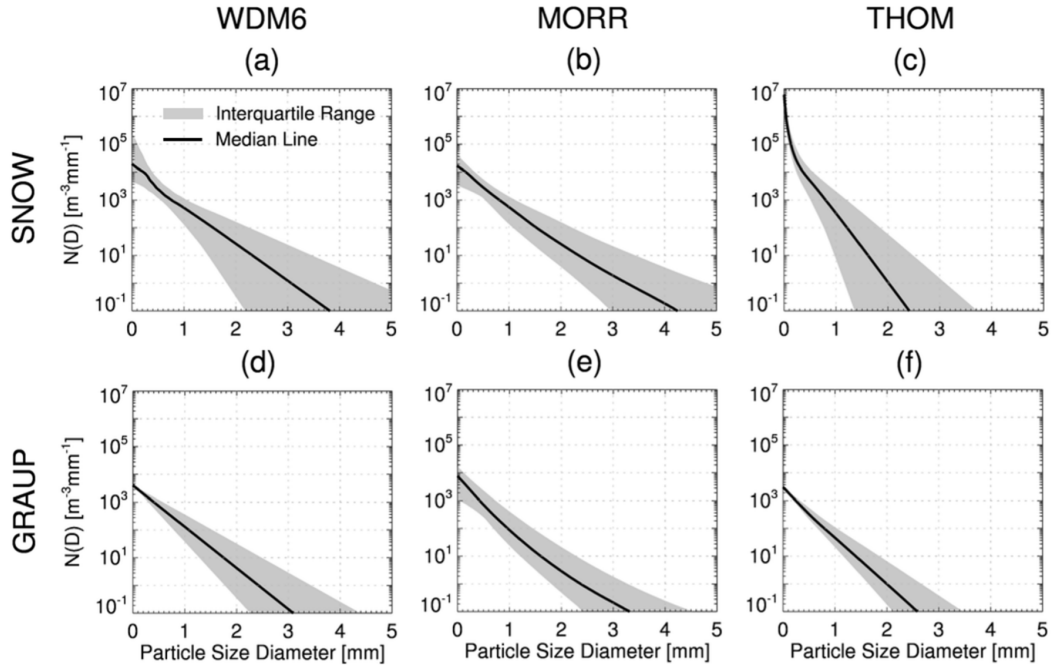
Fig. 6.   Medians (line plot) and interquartile ranges (shadow) of ice PSDs simulated by the bulk schemes (left: WDM6, middle: MORR, and right: THOM) for the tropical cyclone (03:40 UTC August 7, 2019). The first row (a)–(c) shows the snow size distributions and the second row (d)–(f) indicates the graupel size distributions. A minimum threshold value of the ice water content is set to 0.005 g/m^3.
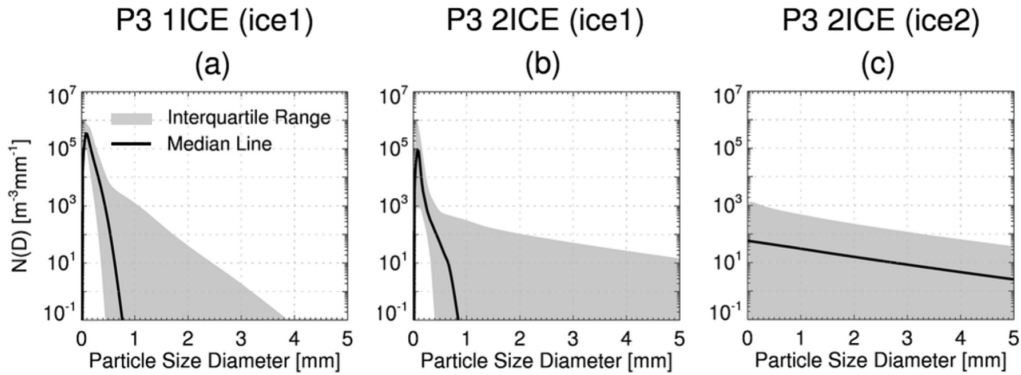

Fig. 7.   Similar to Fig. 6, but for the free ice categories in the P3 scheme. (a) Left image represents the single free category in the P3 1ICE scheme. (b) Middle and (c) right images show the first (ice1) and the second (ice2) free ice categories, respectively, in the P3 2ICE scheme.

become stronger with increasing frequency, but the extent of the change depends on the microphysical assumption and predicted variables. At 37 GHz [Fig. 8(a)], the MORR scheme exhibited the largest TB depression; it fell below 220 K at the center (roughly 144°E) of the strong convection, whereas the other schemes stayed at approximately 230 K or higher. Here, the relatively cold TB signals verify the scattering by large snow particles. Particularly, the MORR scheme, as a typical double-moment scheme, can predict $N_{\text{tot},s}$, which generally tends to be less than that of the other schemes, as demonstrated in studies of [18], [55], and [56]. Furthermore, we compared the diagnosed and predicted $N_{\text{tot},s}$ (Fig. 9). Similarly, the MORR scheme simulated smaller $N_{\text{tot},s}$ than the WDM6 scheme. A small $N_{\text{tot},s}$ directly decreases N_{0s} and λ_s, as discussed and shown in Fig. 3(a), consequently yielding a myriad of large-sized particles [see Fig. 6(b)]. It can be estimated that the notable scattering of the MORR scheme at 37 GHz was caused by the presence of too many large-sized snow particles.

On the contrary, the THOM scheme exhibited the weakest scattering signals at 37 GHz [Fig. 8(a)], despite its highest snow water content [Fig. 4(c)], which can be due to two reasons. The first is that the density is variable and depends on the diameter. As shown in Fig. 2, the THOM snow density is less than 100 kg/m^3 when the diameter is greater than 1.32 mm. Therefore, larger snow particles exhibit a lower scattering efficiency with a variable density than that with a fixed density (i.e., 100 kg/m^3). The second reason is its unique PSD, the super-exponential distribution shown in Figs. 3(a) and 6(c). It assumes an exceptionally small amount of large-sized particles. These two reasons well explain the THOM scheme behavior at 37 GHz.

At 89 GHz [Fig. 8(b)], however, the scattering signal by the THOM scheme was similar to that by the MORR scheme. Their minimum values were less than 240 K. The THOM scheme exhibited a noticeably strong scattering at 166 GHz [Fig. 8(c)]. Furthermore, its lowest TB reached about 180 K, whereas that of the MORR scheme was larger than 220 K.
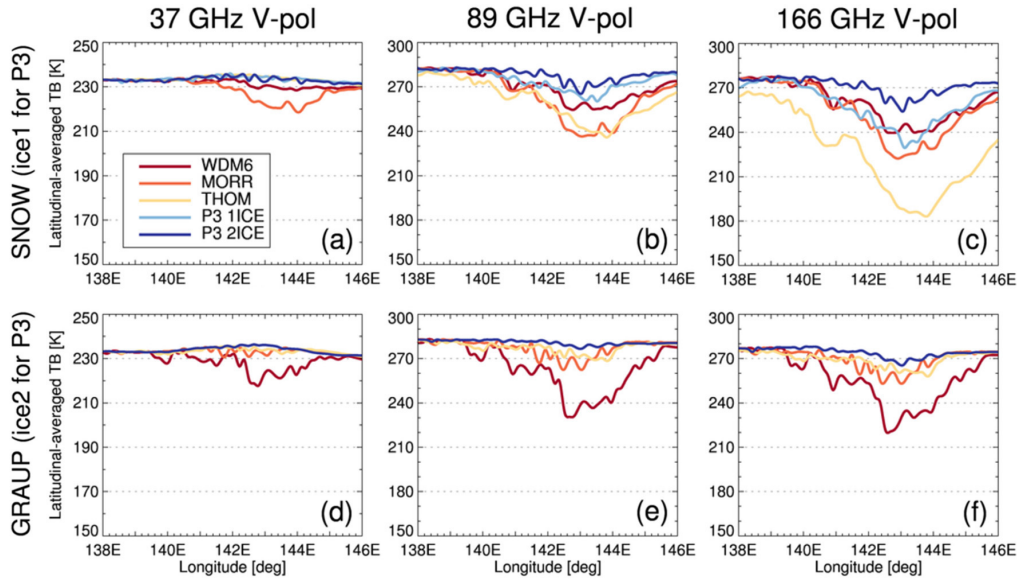
Fig. 8. RTM-simulated TB reductions from the rimed and aggregated ice categories, (a)–(c) snow and (d)–(f) graupel, at the 37, 89, and 166 GHz V-pol channels. The targeted case is the tropical cyclone (03:40 UTC August 7, 2019). The results are averaged in the latitudinal direction. The WRF microphysics parameterization includes the WDM6, MORR, THOM, P3 1ICE, and P3 2ICE schemes (see the legend). Note that the first free ice category (ice1) of the P3 schemes is displayed with snow, and the second free ice category (ice2) of the P3 2ICE scheme is displayed with graupel.
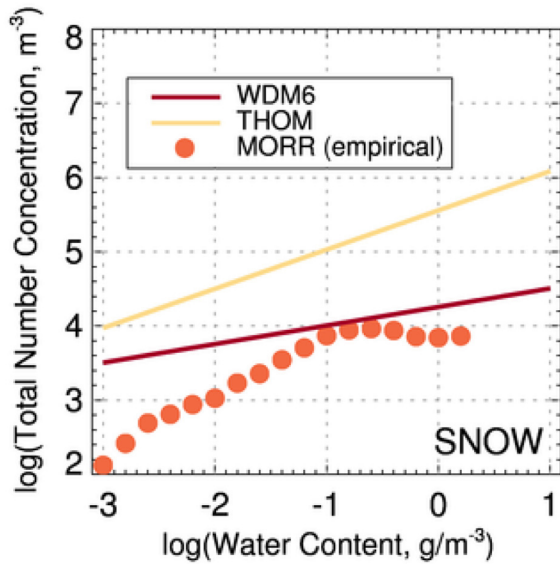

Fig. 9. Log plot of the snow total number concentration, $N_{\text{tot},s}$, versus the snow water content, q_s. The bold lines (WDM6: red line and THOM: yellow line) denote the theoretical relation between the two values, while the orange circle (MORR) indicates an empirical relationship with a bin size of 0.2.

This is because the THOM scheme assumes a high quantity of small-sized snow [see Fig. 6(c)] with a density higher than 100 kg/m³.

Despite comprising high-density ice particles, the P3 schemes generally afford weak scattering signals [Fig. 8(a)–(c)]. Thus, their scattering is insufficient for yielding strong scattering. Moreover, Fig. 8(b) and (c) shows the scattering exhibited by ice1 in the P3 2ICE scheme is weaker than that in the P3 1ICE scheme. The difference was particularly large at 166 GHz. Milbrandt and Morrison [6] noted that the ice parameterization of the P3 2ICE scheme was characterized by a fast growth rate of the particle

size, which mitigated the dilution problem. However, our results show that the fast growth rate also simultaneously significantly reduces the small particles, which is evident by its weakest scattering at 166 GHz.

The second row of Fig. 8 shows the TB depressions by graupel (or ice2 for P3 2ICE). As a high-density particle (400 or 500 kg/m³), graupel ensures good scattering efficiency, but most schemes do not simulate as much graupel as snow (Fig. 4). Fig. 8 shows that scattering from graupel is weaker than that from snow, except for the WDM6 scheme. Only in the WDM6 scheme, graupel is regarded as the most important source of scattering. A major contributor to that strong scattering is the graupel water content predicted by the WDM6 scheme. Actually, it has already been reported as a systematic deficiency in [57], although a further revision [58] has partially alleviated the deficiency. Furthermore, the WDM6 scheme is assumed to possess a density of 500 kg/m³, whereas the MORR and THOM schemes are assumed to possess densities of 400 kg/m³. Understandably, the assumptions reinforce the excessive scattering from the WDM6 graupel. In the THOM scheme, although the rain droplet was artificially eliminated herein, its existence may have contributed in increasing the graupel-induced scattering at 37 GHz because of the rain droplet correction discussed and shown in Fig. 3(b). Fig. 8(d)–(f) shows the scattering signals by the ice2 of the P3 2ICE scheme. It complements ice1 but still exhibits weak scattering. None of the bulk schemes exhibited weaker scattering than that by ice2 of the P3 2ICE scheme.

These results well explain how snow and graupel (or P3 ice) actually contribute to TB depression. The findings are significant as the major differences among the five bulk schemes are mainly in their cold rain processes. However, to properly evaluate the bulk schemes, the observed TBs in all-cloud conditions need to be compared. The results are provided in Section IV-C.
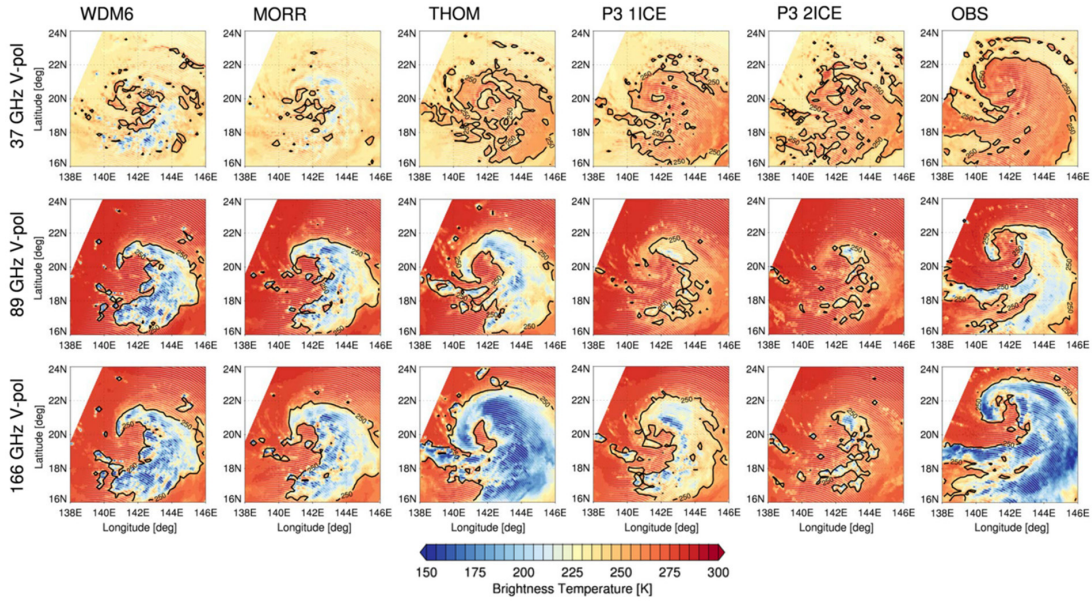
Fig. 10. RTM-simulated TBs (the first–fifth columns) and GMI-observed TBs (the sixth column) at 37, 89, and 166 GHz V-pol channels. The targeted case is the tropical cyclone (03:40 UTC August 7, 2019). The black outline surrounding the tropical cyclone corresponds to a value of 250 K.
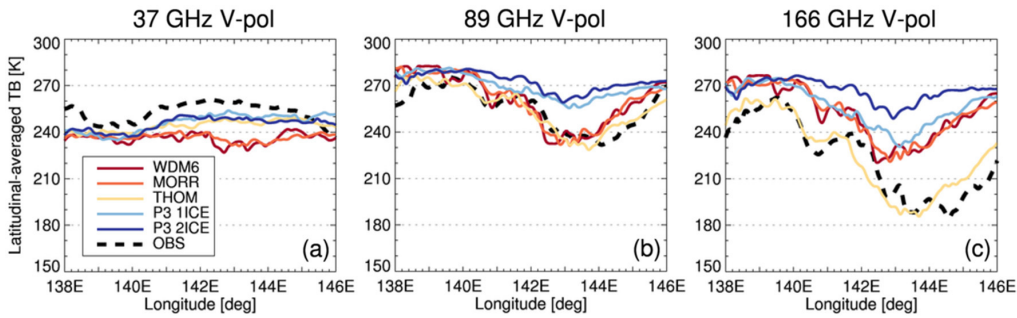

Fig. 11. Similar to Fig. 8, but for the latitudinal-averaged TB attenuation under all cloud conditions with the GPM GMI observation (black dashed line) at (a) 37, (b) 89, and (c) 166 GHz V-pol channels.

C. Direct Comparison With Observations

Herein, we present a comparative evaluation of the TB simulations based on the observed TB under all cloud conditions, including water vapor, liquid water droplets, and ice particles. The results were obtained by passive microwave radiative transfer simulation based on the scheme's own microphysical assumptions and shifted toward the center of GMI's field of view. When both data exist at a given point, they are included in the dataset employed herein. Fig. 10 shows the TB simulations for the WDM6, MORR, THOM, P3 1ICE, and P3 2ICE schemes (first–fifth columns, respectively) and the GMI observation (the last column). As expected, the location and intensity of the tropical cyclones vary, but if the microphysical assumptions are similar to reality, the simulated TB distributions should be as close as possible to those of the observations. At 37 GHz, the WDM6 and MORR schemes possessed cold TB in regions where the observations possessed warm TB induced by the absorption–emission of liquid droplets. At 89 and 166 GHz, the P3 schemes failed to simulate TB depressions corresponding to the observations. On the contrary, the THOM scheme exhibited sufficiently scattered TBs, which is the most similar to the observations, especially at 166 GHz. For more detailed evaluation, we described the

latitudinal averages of the TB dataset at 37, 89, and 166 GHz in Fig. 11 and used the mean bias error (MBE) given in Table IV.

Fig. 11(a) (37 GHz) shows that in the observations (black dashed line), the highest TB (almost 260 K) is at the center of strong precipitation and the lowest TB (less than 240 K) is at the right edge. Its convex shape at the center implies a high emissivity caused by strong wind speeds and more dominant absorption–emission compared to scattering. Similarly, the maximum TB of the P3 schemes (1ICE and 2ICE) (approximately 10 K less than that of the observation) is at the center. The MBEs of the P3 schemes (1ICE and 2ICE) were −5.97 and −6.95 K, respectively. The THOM scheme basically followed the trend of the observations and P3 schemes. However, its MBE was −7.91 K. The three schemes did not significantly simulate the TB reduction by the ice particles at 37 GHz (Fig. 8). Thus, the TB underestimation here was mainly caused by other factors (lack of rain droplets, underestimated surface emissivity, or other model errors).

However, we obtained unexpected scattering signals in the WDM6 and MORR schemes. They afforded substantially negative MBEs (−15.98 and −15.16 K, respectively), which were nearly twice as much as that afforded by the
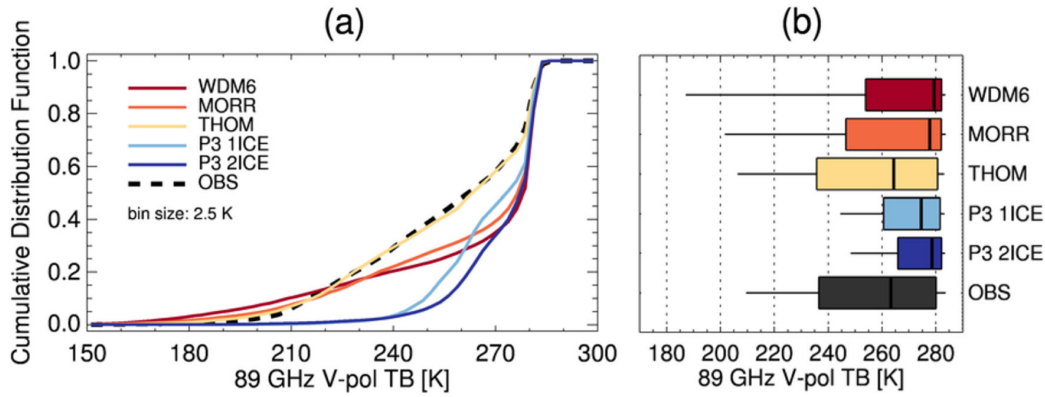
Fig. 12. (a) Empirical CDF (bin size is 2.5 K) and (b) simple box and whisker plot for the RTM-simulated TB and GMI-observed TB at 89 GHz V-pol. In the box plot, the left boundary indicates the 25th percentile; the bold black line within the box marks the median; and the right boundary indicates the 75th percentile. Whiskers on the left and right sides of the box denote the 5th and 95th percentiles, respectively.

TABLE IV
MBE [K] BETWEEN THE RTM-SIMULATED TB AND GMI-OBSERVED TB AT THE 37, 89, AND 166 GHZ V-POL CHANNELS

Scheme	Mean bias error [K]		
	37 GHz V-pol	89 GHz V-pol	166 GHz V-pol
WDM6	−15.98	5.60	29.55
MORR	−15.16	5.82	29.27
THOM	−7.91	0.14	2.61
P3 1ICE	−5.97	13.60	33.35
P3 2ICE	−6.95	16.76	43.15

THOM scheme. Especially, although the observations and other schemes afforded their maximum TBs at the center of strong precipitation, the WDM6 and MORR schemes afforded their minimum TBs (about 230 K) there. These results imply that the WDM6 and MORR schemes overestimate the degree of scattering at 37 GHz. As discussed earlier in the first column of Fig. 8, these results are probably due to the presence of numerous large-sized graupels in the WDM6 scheme and snows in the MORR scheme.

Fig. 11(b) (89 GHz) shows that the observations exhibit a certain sign of scattering, indicating a low peak (nearly 230 K) at 144°E. Moreover, the WDM6, MORR, and THOM schemes afforded TB patterns relatively similar to the observations, and they were less biased at 89 GHz than at 37 GHz (Table IV). For further assessment, we illustrated a cumulative distribution function (CDF) and simple box and whisker plot (down to 5th percentile and up to 95th percentile) in Fig. 12, clearly revealing the embedded problem of the WDM6 and MORR schemes at 89 GHz. Two primary representative discrepancies were observed. First, similar to that at 37 GHz, the schemes overestimated the strong scattering at 89 GHz. Additionally, in the WDM6 and MORR schemes, the top 5% of the strongly scattered TBs was 22.46 and 7.98 K colder than that of the

observations [Fig. 12(b)], respectively. Second, the schemes underestimated the medium and light scattering; their median values were 16.07 and 14.44 K warmer than that of the observations, respectively. Therefore, the WDM6 and MORR schemes contained excessive large-sized ice particles and did not contain sufficient medium- and small-sized ice particles.

On the contrary, the THOM scheme consistently exhibited an extremely similar TB distribution to the observations (Fig. 12). Although it slightly overestimated the strong scattering, it was not greater than the overestimation of the WDM6 and MORR schemes. The super-exponential distribution helped the THOM scheme to not simulate extremely large-sized snow particles. Furthermore, the diameter-dependent snow density probably contributed to the good agreement. To analyze the effectiveness of the diameter-dependent density in the THOM scheme, we calculated a CDF of 89 GHz TBs using the fixed snow density of 100 kg/m^3 and compared it to the original CDF (Fig. 13). The diameter-dependent snow density decreased the percentage of strong scattering below 230 K and increased the percentage of medium and light scattering above 230 K. The difference of CDFs due to the density assumption is bigger at the 166-GHz channel (not shown here). In general, the diameter-dependent
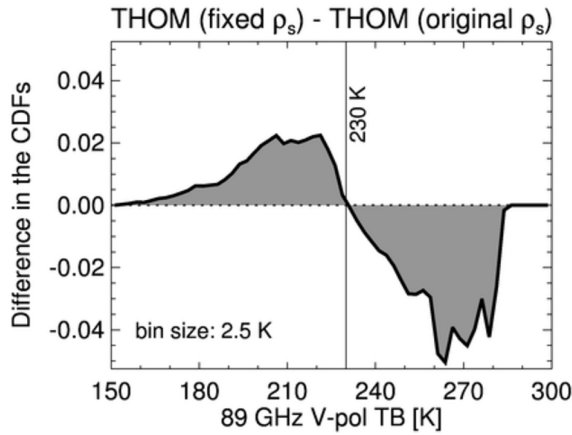
Fig. 13.   THOM snow density effects on the empirical CDF (bin size is 2.5 K). The difference signifies the CDF of the fixed density ($\rho_s = 100$ kg/m^3) minus the CDF of the diameter-dependent (original) density.

density helps to simulate sufficient scattering signals from small-sized snow particles. Therefore, the diameter-dependent snow density could be considered a good factor for reducing the discrepancies between the simulations and observations. On the contrary, the P3 schemes were heavily biased toward warm TBs (13.60 and 16.76 K; Table IV) at 89 GHz, although their assumptions of the diameter-dependent ice density were similar to that of the THOM snow. The insufficient scattering signals were perhaps due to the limitation of the insufficient simulation of large-sized ice particles.

The differences among the simulations became clear at 166 GHz [Fig. 11(c)], which could be efficiently scattered by small particles. The THOM scheme was almost the only scheme to exhibit scattering signals similar to the observations, and its MBE was 2.61 K. However, the WDM6 and MORR schemes did not exhibit similar scattering. They exhibited considerable warm biases of more than 29 K, which is because of their lack of small-sized ice particles (especially snow). Moreover, the P3 schemes exhibited low scattering intensities with the highest MBE scores (more than 33 K). Furthermore, the difference between the two P3 schemes was greater at 166 GHz than that at 89 GHz. Since simulations at 166 GHz were more sensitive to small particles, we can conclude that few small-sized ice particles were present in the P3 2ICE scheme. Paradoxically, this result appears to be due to the promoted growth to a large-sized particle, although it is considered a solution to the dilution problem. In other words, the P3 2ICE scheme affords little more large-sized ice particles through a large sacrifice of small particles. Thus, this approach simulates particularly different results from the actual ice size distribution.

Consequently, herein, THOM's ice phase microphysical assumptions are considered to be the most similar to the actual cloud when evaluated based on the GMI observed TBs, especially at the scattering channels (37, 89, and 166 GHz). Its snow assumption is especially valid. On the contrary, the evaluation results of the WDM6 and MORR schemes raised three concerns: 1) excessive amount of large-sized ice particles; 2) shortage of small-sized ice particles; and 3) fixed density. The P3 schemes did not possess sufficient

(small-to-large) ice particles for strong scattering. Finally, the P3 2ICE performance was bad because of its small-sized particle loss problem.

Although only a specific tropical cyclone case of the western Pacific Ocean was targeted herein, sufficient evidence was obtained to deduce that these results are induced by the general nature of the microphysical assumptions in the bulk schemes. This was possible through the implementation of the microphysical-consistent RTM that fully considers the density and PSD. Consequently, our findings suggest that matching the RTM's microphysical assumptions with those of the model being referenced is essential.

V. Conclusion

This study aimed to implement a passive microwave RTM that considers various microphysical assumptions of bulk schemes. For this, we created a Mie scattering LUT comprising all the state vectors needed to represent the assumptions. Although the Mie assumption was applied for nonspherical particles, if particle density decreases exponentially with diameter, it is considered a relatively smaller error source than the other microphysics assumptions [30]. This study also aimed to evaluate the microphysical assumptions based on the passive microwave radiative transfer simulation. Five bulk schemes (WDM6, MORR, THOM, P3 1ICE, and P3 2ICE) in the WRF model were used to yield input variables for the radiative transfer simulation. The aim was to match the microphysical assumptions of the radiative transfer simulation to those of the bulk schemes. Particularly, this study emphasized that the passive microwave RTM possesses a strong advantage as it can handle multiple scattering channels (e.g., 37, 89, and 166 GHz). This allowed us to evaluate the effect of different particle sizes on microwave scattering. This study focused on rimed and aggregated ice categories (snow, graupel, and P3 ice), which are important particles for the scattering channels. The signal-based evaluation was carried out for the tropical cyclone "Krosa" (2019) observed by the GPM GMI.

Several issues were discussed for the ice-phase microphysical assumption of the bulk schemes through intensity, distribution, and statistical measures of simulated TBs. First, in the WDM6 and MORR schemes, the overestimation of the scattering degree at 37 GHz implies that the schemes tend to overestimate the number of large-sized ice particles (graupel in the WDM6 scheme and snow in the MORR scheme). On the contrary, the opposing results at 166 GHz indicate that the schemes underestimate the number of small-sized ice particles. Furthermore, assuming fixed snow density may be invalid because it widens the gap between the simulated and observed TBs. Second, the THOM scheme exhibited the most similar TB distributions to the observations in the scattering channels above 89 GHz. Its MBE scores (0.14 K for 89 GHz and 2.61 K for 166 GHz) also well support this evidence. Hence, we suggest that the ice-phase microphysical assumptions of the THOM scheme are most similar to those of reality, at least for the case considered. Particularly, the diameter-dependent snow density and its super-exponential distribution contributed to the favorable evaluation. Third, the P3 schemes (1ICE and 2ICE) afforded significantly inadequate scattering signals

at 89 GHz and above, denoting that the number of ice particles was generally underestimated regardless of the particle size. Although the P3 2ICE scheme is considered a solution to the dilution problem, it simulated considerably weaker scattering signals than the P3 1ICE scheme, especially at 166 GHz. We indicated that this is mainly responsible for the lack of small-sized ice particles in the P3 2ICE approach. In other words, the P3 2ICE scheme sacrificed too many small-sized ice particles to afford a few large-sized ice particles, yielding unsatisfactory results.

This study provides the first TB-based assessment of the bulk schemes with flexible ice density, which was enabled by the implementation of the microphysical-consistent radiative transfer simulation. However, it is undeniable that our results contain some errors related to particle shape and dielectric constant, as the Mie assumption is applied for nonspherical particles. Furthermore, the scope of this study was restricted to the evaluation of the WRF simulation for the instantaneous sample. A major limitation of this method is that evaluating the consequence of the interaction among the hydrometeors (vapor, liquid water droplets, and ice particles) at all consecutive time steps is difficult. Therefore, the modification of the PSD parameters (N_0, λ, and μ) or density is not possible without more comprehensive analysis. Similarly, the microphysical assumption within the RTM should be handled in combination with the cloud-resolving model.

Notwithstanding this limitation, this study provides valuable information about several ice-related microphysical assumptions. Furthermore, the study's findings can be used for comprehensive purposes, such as an all-sky data assimilation system and satellite instrument retrieval algorithms based on *a priori* knowledge. Therefore, continued efforts are required to minimize the unreasonable microphysical assumption in the passive microwave RTM.

REFERENCES

[1] A. P. Khain *et al.*, "Representation of microphysical processes in cloud-resolving models: Spectral (bin) microphysics versus bulk parameterization," *Rev. Geophys.*, vol. 53, no. 2, pp. 247–322, Jun. 2015.

[2] H. Morrison, J. A. Curry, and V. I. Khvorostyanov, "A new double-moment microphysics parameterization for application in cloud and climate models. Part I: Description," *J. Atmos. Sci.*, vol. 62, no. 6, pp. 1665–1677, Jun. 2005.

[3] G. Thompson, P. R. Field, R. M. Rasmussen, and W. D. Hall, "Explicit forecasts of winter precipitation using an improved bulk microphysics scheme. Part II: Implementation of a new snow parameterization," *Mon. Weather Rev.*, vol. 136, no. 12, pp. 5095–5115, 2008.

[4] K.-S. S. Lim and S.-Y. Hong, "Development of an effective double-moment cloud microphysics scheme with prognostic cloud condensation nuclei (CCN) for weather and climate models," *Monthly Weather Rev.*, vol. 138, no. 5, pp. 1587–1612, May 2010.

[5] H. Morrison and J. A. Milbrandt, "Parameterization of cloud microphysics based on the prediction of bulk ice particle properties. Part I: Scheme description and idealized tests," *J. Atmos. Sci.*, vol. 72, no. 1, pp. 287–311, Jan. 2015.

[6] J. A. Milbrandt and H. Morrison, "Parameterization of cloud microphysics based on the prediction of bulk ice particle properties. Part III: Introduction of multiple free categories," *J. Atmos. Sci.*, vol. 73, no. 3, pp. 975–995, Mar. 2016.

[7] G. M. Skofronick-Jackson, A. J. Gasiewski, and J. R. Wang, "Influence of microphysical cloud parameterizations on microwave brightness temperatures," *IEEE Trans. Geosci. Remote Sens.*, vol. 40, no. 1, pp. 187–196, Jan. 2002.

[8] C. Mätzler, "Radiative transfer models for microwave radiometry, COST action 712: Application of microwave radiometry to atmospheric research and monitoring, project 1: Development of radiative transfer models," Eur. Commission, Brussels, Belgium, Final Rep. EUR 19543, 2000.

[9] A. M. Doherty, T. R. Sreerekha, U. M. O'Keeffe, and S. J. English, "Ice hydrometeor microphysical assumptions in radiative transfer models at AMSU-B frequencies," *Quart. J. Roy. Meteorol. Soc.*, vol. 133, no. 626, pp. 1205–1212, 2007.

[10] S. B. Sieron, E. E. Clothiaux, F. Zhang, Y. Lu, and J. A. Otkin, "Comparison of using distribution-specific versus effective radius methods for hydrometeor single-scattering properties for all-sky microwave satellite radiance simulations with different microphysics parameterization schemes," *J. Geophys. Res., Atmos.*, vol. 122, no. 13, pp. 7027–7046, Jul. 2017.

[11] J. L. Bytheway and C. D. Kummerow, "Consistency between convection allowing model output and passive microwave satellite observations," *J. Geophys. Res., Atmos.*, vol. 123, no. 2, pp. 1065–1078, Jan. 2018.

[12] S. English, P. Lean, and A. Geer, "How radiative transfer models can support the future needs of Earth-system forecasting and re-analysis," *J. Quant. Spectrosc. Radiat. Transf.*, vol. 251, Aug. 2020, Art. no. 107044.

[13] H. Masunaga, M. Satoh, and H. Miura, "A joint satellite and global cloud-resolving model analysis of a Madden–Julian oscillation event: Model diagnosis," *J. Geophys. Res.*, vol. 113, no. D17, pp. 1–11, 2008.

[14] T. Matsui, X. Zeng, W.-K. Tao, H. Masunaga, W. S. Olson, and S. Lang, "Evaluation of long-term cloud-resolving model simulations using satellite radiance observations and multifrequency satellite simulators," *J. Atmos. Ocean. Technol.*, vol. 26, no. 7, pp. 1261–1274, Jul. 2009.

[15] T. Matsui *et al.*, "Introducing multisensor satellite radiance-based evaluation for regional Earth system modeling," *J. Geophys. Res., Atmos.*, vol. 119, no. 13, pp. 8450–8475, Jul. 2014.

[16] J. J. Shi *et al.*, "WRF simulations of the 20–22 January 2007 snow events over eastern Canada: Comparison with *in situ* and satellite observations," *J. Appl. Meteorol. Climatol.*, vol. 49, no. 11, pp. 2246–2266, Nov. 2010.

[17] T. Iguchi *et al.*, "Evaluation of cloud microphysics in JMA-NHM simulations using bin or bulk microphysical schemes through comparison with cloud radar observations," *J. Atmos. Sci.*, vol. 69, no. 8, pp. 2566–2586, Aug. 2012.

[18] M. Han, S. A. Braun, T. Matsui, and C. R. Williams, "Evaluation of cloud microphysics schemes in simulations of a winter storm using radar and radiometer measurements," *J. Geophys. Res., Atmos.*, vol. 118, no. 3, pp. 1401–1419, Feb. 2013.

[19] M. Han, S. A. Braun, T. Matsui, and T. Iguchi, "Comparisons of bin and bulk microphysics schemes in simulations of topographic winter precipitation with radar and radiometer measurements," *Quart. J. Roy. Meteorol. Soc.*, vol. 144, no. 715, pp. 1926–1946, Jul. 2018.

[20] V. S. Galligani, D. Wang, M. A. Imaz, P. Salio, and C. Prigent, "Analysis and evaluation of WRF microphysical schemes for deep moist convection over south-eastern South America (SESA) using microwave satellite observations and radiative transfer simulations," *Atmos. Meas. Techn.*, vol. 10, no. 10, pp. 3627–3649, Oct. 2017.

[21] S. B. Sieron, F. Zhang, E. E. Clothiaux, L. N. Zhang, and Y. Lu, "Representing precipitation ice species with both spherical and nonspherical particles for radiative transfer modeling of microphysics-consistent cloud microwave scattering properties," *J. Adv. Model. Earth Syst.*, vol. 10, no. 4, pp. 1011–1028, Apr. 2018.

[22] D. Ori and S. Kneifel, "Assessing the uncertainties of the discrete dipole approximation in case of melting ice particles," *J. Quant. Spectrosc. Radiat. Transf.*, vol. 217, pp. 396–406, Sep. 2018.

[23] R. J. Hogan and C. D. Westbrook, "Equation for the microwave backscatter cross section of aggregate snowflakes using the self-similar Rayleigh–Gans approximation," *J. Atmos. Sci.*, vol. 71, no. 9, pp. 3292–3301, Sep. 2014.

[24] R. J. Hogan, R. Honeyager, J. Tyynelä, and S. Kneifel, "Calculating the millimetre-wave scattering phase function of snowflakes using the self-similar Rayleigh–Gans approximation," *Quart. J. Roy. Meteorol. Soc.*, vol. 143, no. 703, pp. 834–844, Jan. 2017.

[25] M. S. Kulie, R. Bennartz, T. J. Greenwald, Y. Chen, and F. Weng, "Uncertainties in microwave properties of frozen precipitation: Implications for remote sensing and data assimilation," *J. Atmos. Sci.*, vol. 67, no. 11, pp. 3471–3487, 2010.

[26] H. Nowell, G. Liu, and R. Honeyager, "Modeling the microwave single-scattering properties of aggregate snowflakes," *J. Geophys. Res., Atmos.*, vol. 118, no. 14, pp. 7873–7885, Jul. 2013.

[27] K.-S. Kuo *et al.*, "The microwave radiative properties of falling snow derived from nonspherical ice particle models. Part I: An extensive database of simulated pristine crystals and aggregate particles, and their scattering properties," *J. Appl. Meteorol. Climatol.*, vol. 55, no. 3, pp. 691–708, Mar. 2016.

[28] W. S. Olson *et al.*, "The microwave radiative properties of falling snow derived from nonspherical ice particle models. Part II: Initial testing using radar, radiometer and *in situ* observations," *J. Appl. Meteorol. Climatol.*, vol. 55, no. 3, pp. 709–722, Mar. 2016.

[29] S. Ringerud, M. S. Kulie, D. L. Randel, G. M. Skofronick-Jackson, and C. D. Kummerow, "Effects of ice particle representation on passive microwave precipitation retrieval in a Bayesian scheme," *IEEE Trans. Geosci. Remote Sens.*, vol. 57, no. 6, pp. 3619–3632, Jun. 2019.

[30] S. Kneifel *et al.*, "Summer snowfall workshop: Scattering properties of realistic frozen hydrometeors from simulations and observations, as well as defining a new standard for scattering databases," *Bull. Amer. Meteorol. Soc.*, vol. 99, no. 3, pp. ES55–ES58, Mar. 2018.

[31] A. J. Geer and F. Baordo, "Improved scattering radiative transfer for frozen hydrometeors at microwave frequencies," *Atmos. Meas. Techn.*, vol. 7, no. 6, pp. 1839–1860, 2014.

[32] S. Q. Zhang, T. Matsui, S. Cheung, M. Zupanski, and C. Peters-Lidard, "Impact of assimilated precipitation-sensitive radiances on the NU-WRF simulation of the West African monsoon," *Monthly Weather Rev.*, vol. 145, no. 9, pp. 3881–3900, Sep. 2017.

[33] A. J. Geer *et al.*, "All-sky satellite data assimilation at operational weather forecasting centres," *Quart. J. Roy. Meteorol. Soc.*, vol. 144, no. 713, pp. 1191–1217, Apr. 2018.

[34] C. Kummerow, "On the accuracy of the Eddington approximation for radiative transfer in the microwave frequencies," *J. Geophys. Res., Atmos.*, vol. 98, no. D2, pp. 2757–2765, Feb. 1993.

[35] H. J. Liebe, G. A. Hufford, and M. G. Cotton, "Propagation modeling of moist air and suspended water/ice particles at frequencies below 1000 GHz," in *Proc. AGARD 52nd Spec. Meeting Electromagn. Wave Propag. Panel Symp.*, Palma de Mallorca, Spain, May 1993, pp. 1–10.

[36] M. Kazumori and S. J. English, "Use of the ocean surface wind direction signal in microwave radiance assimilation," *Quart. J. Roy. Meteorol. Soc.*, vol. 141, no. 689, pp. 1354–1375, Apr. 2015.

[37] R. Saunders *et al.*, "An update on the RTTOV fast radiative transfer model (currently at version 12)," *Geosci. Model Develop.*, vol. 11, no. 7, pp. 2717–2737, 2018.

[38] F. Weng, "Advances in radiative transfer modeling in support of satellite data assimilation," *J. Atmos. Sci.*, vol. 64, no. 11, pp. 3799–3807, 2007.

[39] B. Johnson, T. Zhu, M. Chen, Y. Ma, and T. Auligné, "The community radiative transfer model (CRTM)," in *Proc. 21st Int. TOVS Study Conf.*, Darmstadt, Germany, Nov. 2017, pp. 1–24.

[40] P. Bauer, "Including a melting layer in microwave radiative transfer simulation for clouds," *Atmos. Res.*, vol. 57, no. 1, pp. 9–30, Feb. 2001.

[41] R. Grainger, J. Lucas, G. E. Thomas, and G. Ewen, "Calculation of Mie derivatives," *Appl. Opt.*, vol. 43, no. 28, pp. 5386–5393, 2004.

[42] C. F. Bohren and D. R. Huffman, *Absorption and Scattering of Light by Small Particles*. Hoboken, NJ, USA: Wiley, 2008.

[43] A. J. Geer, P. Bauer, and C. W. O'Dell, "A revised cloud overlap scheme for fast microwave radiative transfer in rain and cloud," *J. Appl. Meteorol. Climatol.*, vol. 48, no. 11, pp. 2257–2270, Nov. 2009.

[44] A. J. Heymsfield and J. Iaquinta, "Cirrus crystal terminal velocities," *J. Atmos. Sci.*, vol. 57, no. 7, pp. 916–938, Apr. 2000.

[45] S.-Y. Hong and J.-O. J. Lim, "The WRF single-moment 6-class microphysics scheme (WSM6)," *Asia–Pacific J. Atmos. Sci.*, vol. 42, no. 2, pp. 129–151, 2006.

[46] H. Morrison, J. A. Milbrandt, G. H. Bryan, K. Ikeda, S. A. Tessendorf, and G. Thompson, "Parameterization of cloud microphysics based on the prediction of bulk ice particle properties. Part II: Case study comparisons with observations and other schemes," *J. Atmos. Sci.*, vol. 72, no. 1, pp. 312–339, Jan. 2015.

[47] G. P. Cox, "Modelling precipitation in frontal rainbands," *Quart. J. Roy. Meteorol. Soc.*, vol. 114, no. 479, pp. 115–127, Dec. 2006.

[48] P. R. A. Brown and P. N. Francis, "Improved measurements of the ice water content in cirrus using a total-water probe," *J. Atmos. Ocean. Technol.*, vol. 12, no. 2, pp. 410–414, Apr. 1995.

[49] P. R. Field, R. J. Hogan, P. R. A. Brown, A. J. Illingworth, T. W. Choularton, and R. J. Cotton, "Parametrization of ice-particle size distributions for mid-latitude stratiform cloud," *Quart. J. Roy. Meteorol. Soc.*, vol. 131, no. 609, pp. 1997–2017, Jul. 2005.

[50] P. R. Field, A. J. Heymsfield, and A. Bansemer, "Snow size distribution parameterization for midlatitude and tropical ice clouds," *J. Atmos. Sci.*, vol. 64, no. 12, pp. 4346–4365, Dec. 2007.

[51] T. R. Knutson, J. J. Sirutis, S. T. Garner, I. M. Held, and R. E. Tuleya, "Simulation of the recent multidecadal increase of Atlantic hurricane activity using an 18-km-grid regional model," *Bull. Amer. Meteorol. Soc.*, vol. 88, no. 10, pp. 1549–1565, Oct. 2007.

[52] X. Li and Z. Pu, "Sensitivity of numerical simulation of early rapid intensification of Hurricane Emily (2005) to cloud microphysical and planetary boundary layer parameterizations," *Monthly Weather Rev.*, vol. 136, no. 12, pp. 4819–4838, Dec. 2008.

[53] W.-K. Tao *et al.*, "The impact of microphysical schemes on hurricane intensity and track," *Asia–Pacific J. Atmos. Sci.*, vol. 47, no. 1, pp. 1–16, Jan. 2011.

[54] J.-H. Kim, D.-B. Shin, and C. Kummerow, "Impacts of *a priori* databases using six WRF microphysics schemes on passive microwave rainfall retrievals," *J. Atmos. Ocean. Technol.*, vol. 30, no. 10, pp. 2367–2381, Oct. 2013.

[55] A. Solomon, H. Morrison, O. Persson, M. D. Shupe, and J.-W. Bao, "Investigation of microphysical parameterizations of snow and ice in Arctic clouds during M-PACE through model–observation comparisons," *Monthly Weather Rev.*, vol. 137, no. 9, pp. 3110–3128, Sep. 2009.

[56] A. L. Molthan and B. A. Colle, "Comparisons of single- and double-moment microphysics schemes in the simulation of a synoptic-scale snowfall event," *Monthly Weather Rev.*, vol. 140, no. 9, pp. 2982–3002, Sep. 2012.

[57] Y. Lin and B. A. Colle, "The 4–5 December 2001 IMPROVE-2 event: Observed microphysics and comparisons with the weather research and forecasting model," *Monthly Weather Rev.*, vol. 137, no. 4, pp. 1372–1392, Apr. 2009.

[58] S.-Y. Hong *et al.*, "Evaluation of the WRF double-moment 6-class microphysics scheme for precipitating convection," *Adv. Meteorol.*, vol. 2010, pp. 1–10, Jan. 2010.

Jiseob Kim was born in Kangwon, South Korea, in 1991. He received the B.S. degree in atmospheric sciences from Yonsei University, Seoul, South Korea, in 2016, where he is currently pursuing the Ph.D. degree.

His research interests include passive microwave rainfall retrievals and polarized microwave radiative transfer processes with multiple scattering from inhomogeneous hydrometeors.

Dong-Bin Shin received the B.S. and M.S. degrees in atmospheric sciences from Yonsei University, Seoul, South Korea, in 1987 and 1989, respectively, and the Ph.D. degree in atmospheric sciences from Texas A&M University, College Station, TX, USA, in 1999.

He was a Research Professor with the Center for Earth Observing and Space Research, School of Computational Sciences, George Mason University, Fairfax, VA, USA, and the Department of Atmospheric Science, Colorado State University, Fort Collins, CO, USA, as a Research Associate, from 2000 to 2007. He is currently with the Department of Atmospheric Sciences, Yonsei University, where he has been first an Associate Professor then a Professor since 2007. His research interests include physically based remote sensing of clouds and precipitation from infrared and microwave observations and radiative transfer modeling. His research also focuses on understanding global and regional hydrological balances.

Donghyeck Kim was born in Busan, South Korea, in 1993. He received the B.S degree in atmospheric sciences from Yonsei University, Soul, South Korea, in 2018, where he is currently pursuing the Ph.D. degree.

His research interests include the dynamic phenomena shown by satellite latent heating estimation and the passive microwave latent heating retrievals.